Influence of the Inclusion Shape on the Rolling Contact Fatigue Life of Carburized Steels

YUTAKA NEISHI, TAIZO MAKINO, NAOKI MATSUI, HITOSHI MATSUMOTO, MASASHI HIGASHIDA, and HIDETAKA AMBAI

It has been well known that the flaking failure in rolling contact fatigue (RCF) originates from nonmetallic inclusions in steels, and their apparent size is one of the important factors affecting RCF life. However, the influence of inclusion shape on the RCF life has not been fully clarified. In this study, attention was paid to the influence of the inclusion shape on the RCF life. This was evaluated by using carburized JIS-SCM420 (SAE4320) steels that contained two different shapes of MnS—stringer type and spheroidized type—as inclusions. Sectional observations were made to investigate the relation between the occurrence of shear crack in the subsurface and the shape of MnS. It was found that the RCF life was well correlated with the length of MnS projected to the load axis, and the initiation of shear crack in subsurface was accelerated as the length of MnS increased.

DOI: 10.1007/s11661-012-1344-9

I. INTRODUCTION

RECENTLY, there is an increasing demand for reduction of CO_2 emission to protect the environment. To solve the problem for CO_2 emission, it is important for steel products to be energy saving, compact, and lightweight. Bearings are one of the automotive parts subjected to rolling and sliding contact under high loaded conditions. To realize the need to be compact and lightweight, the fatigue strength of bearings, especially rolling contact fatigue (RCF) strength, must be improved. It has been well known that the flaking failure in RCF originates from nonmetallic inclusions in steels,[1] and the oxide inclusions are harmful to the RCF life.[2–9] Therefore, many studies[10–17] have been carried out to clarify the effect of oxide size,[10,11] oxide composition,[12–14] and matrix–oxide interface condition[2,14–16] on RCF life.

For example, Nagao *et al.*[17] studied the relationship between the RCF life and the maximum inclusion square root area calculated by the statistics of extreme value. They suggested that the calculated maximum inclusion size was the dominant factor in the RCF life regardless of the inclusion type. Hashimoto *et al.*[15] investigated the relationship between the RCF life and the oxide composition and matrix–oxide interface condition. They indicated that the oxide inclusion/matrix interface cavities were created during plastic deformation, and the fatigue crack was initiated from the cavities at the early stage of RCF life due to the local stress magnitude induced around the oxide inclusion/matrix interface enlarged. According to the previous results, the RCF life was improved by reducing the oxide size and the cavities, and by tuning the chemical composition of oxide. In the RCF life of a material containing similar sized oxide, the chemical composition is the more affecting factor.

Moreover, many finite elements models for material fatigue localized around inclusions have been developed to make clear the quantitatively effect of material parameter on the crack initiation and propagation in rolling contact.[18–24]

Based on these results, the total amount of oxygen content in steels for bearing use has been reduced remarkably by improvements in steel production processes. As a consequence, the quality of cleanliness for the bearing steel has been improved, and the RCF life of steels has been prolonged every year.

On the other hand, decreasing the amount of oxide in steel has caused another problem in which another inclusion such as MnS may grow larger than the oxide. To ensure the excellent RCF life, the effect of the MnS shape on the RCF life should be clearly understood because MnS is a deformable inclusion. However, there is little research regarding the MnS shape effect on the RCF life.[25–29] It is assumed that the influence of sulphides (MnS) on the RCF life is similar to that of oxides. The remarkable features of sulfides are as follows: (1) deformable inclusion and (2) no inclusion/matrix interface cavities are present around sulfides.[15]

In this study, attention was paid to the influence of the inclusion shape on the RCF life. This was evaluated by using carburized JIS-SCM420 (SAE4320) steels that contained two different shapes of MnS—stringer type and spheroidized type—as inclusions. Sectional

YUTAKA NEISHI, TAIZO MAKINO, and NAOKI MATSUI, Senior Research Engineers, are with the Corporate Research & Development Laboratories, Sumitomo Metal Industries, Ltd., Amagasaki, Hyogo 660-0891, Japan. Contact e-mail: neishi-ytk@sumitomometals.co.jp HITOSHI MATSUMOTO, Group Manager, MASASHI HIGASHIDA, Assistant Manager, and HIDETAKA AMBAI, Research Engineer, are with the Products Development Department, Kokura Steel Works, Bar & Wire Rod Company, Sumitomo Metal Industries, Ltd.

Manuscript submitted April 13, 2012.
Article published online August 15, 2012

observations were made to investigate the relation between the occurrence of shear crack in the subsurface and the shape of MnS. It was found that the RCF life was well correlated with the length of MnS projected to the load axis, and the initiation of shear crack in the subsurface was accelerated as the length of MnS increased.

II. EXPERIMENTAL PROCEDURE

A. *Material*

In order to understand the influence of the inclusion shape on the RCF life, carburized JIS-SCM420 (SAE4320 equivalent) steels that contained two different shapes of MnS have been prepared. Steel A contained stringer-type MnS and steel B contained spheroidized-type MnS. Two different steels were produced by vacuum-induction melting, and their ingots were forged at 1523 K (1250 °C) into 80-mm-diameter bars. The forged bars were normalized at 1173 K (900 °C) for 3.6 ks. The chemical compositions of both steels are given in Table I, and the typical shapes of MnS observed in the forged bars are shown in Figure 1.

After the normalized treatment, the forged bars were machined into two different types of specimens: for the RCF test and for the ultrasonic fatigue test. The dimensions of each test specimen are illustrated in Figure 2. RCF test specimens were taken from the center of the forged bar in the longitudinal direction. On the other hand, ultrasonic fatigue test specimens were taken from the middle portion of the forged bar in the transverse direction.

Both specimens were gas carburized at 1203 K (930 °C) for 32.4 ks in a sealed quench furnace to a surface carbon content of 0.8 pct, and then these specimens were directly quenched in oil from 1093 K (820 °C). After quenching, all specimens were tempered at 453 K (180 °C) for 7.2 ks. The schematic illustration of heat pattern of gas carburizing and tempering is shown in Figure 3. The hardened specimens were finished to the final shape as shown in Figure 2.

The hardness profiles of the RCF test specimens are shown in Figure 4. The hardness profile was measured in the plane that was parallel to the tangential line of the rolling track center. Hard layer thickness is defined as the depth from the surface where hardness reaches a value of 550 HV. The surface hardness of the specimens was around 750 HV and the hard layer thickness was 1.5 mm for each steels.

The gas-carburizing and tempering treatment develops the residual stress at the surface of the specimen. The residual stress distribution in the subsurface of specimens was measured by X-ray diffraction method. A Rigaku PSPC-RSF diffractometer with a CrKα radiation tube was used. Residual stress was measured in circumferential direction. Residual stresses were measured at the exposed surface and five different depths: 10, 30, 50, 100, and 200 μm below the surface. The residual stress distributions are shown in Figure 5.

Residual stresses of both steel specimens showed similar distribution, and the value of stress at all depths is compressive. Therefore, it was concluded that even if

Table I. Chemical Composition of Steels (Mass Percent)

Mark	C	Si	Mn	P	S	Cr	Mo	Ca
Steel A	0.20	0.19	0.78	0.015	0.018	1.18	0.20	—
Steel B	0.20	0.19	0.78	0.013	0.017	1.18	0.19	0.0026

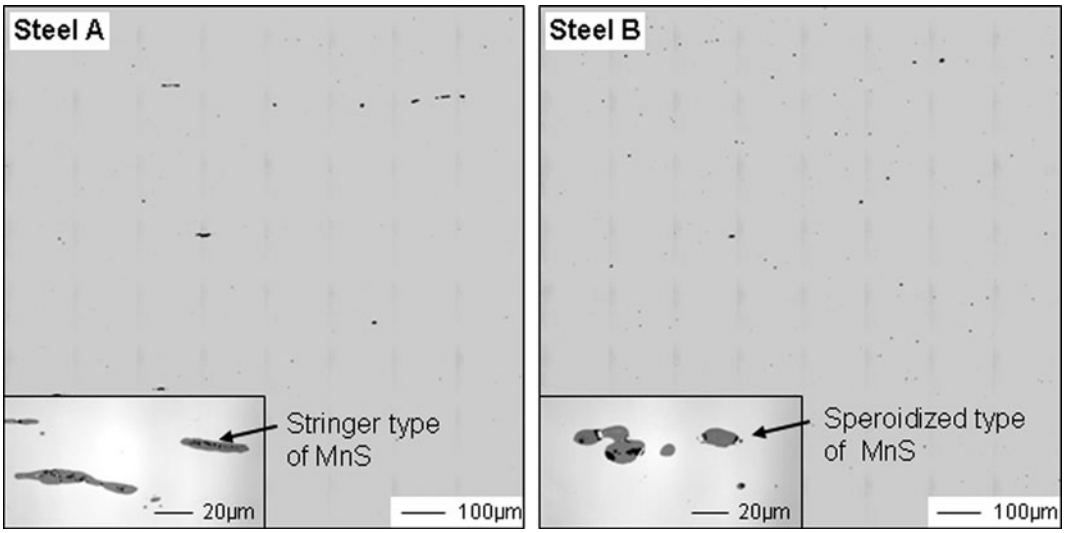

Fig. 1—Optical micrographs of typical shapes of MnS inclusion.

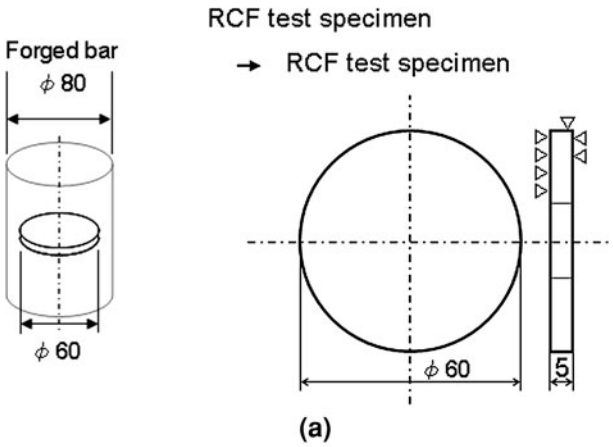

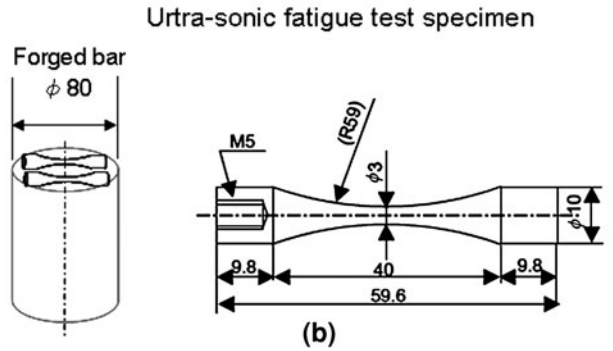

Fig. 2—Dimensions of test specimens: (*a*) RCF test specimen and (*b*) ultrasonic fatigue test.

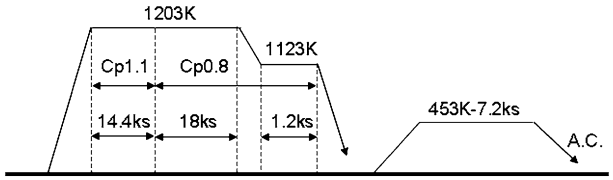

Fig. 3—Schematic illustration of heat pattern of gas carburizing and tempering.

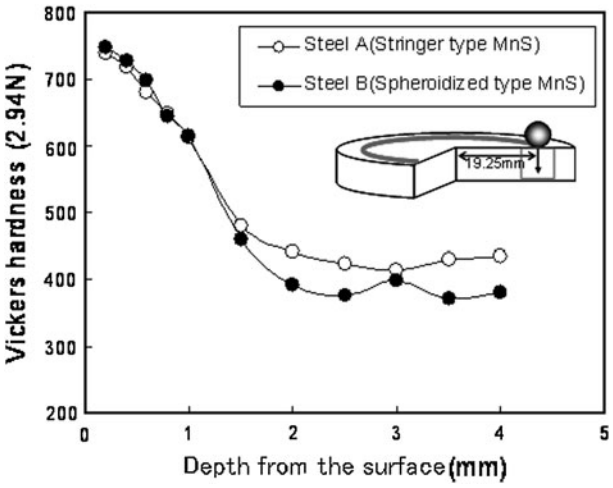

Fig. 4—Hardness profiles of RCF test specimens.

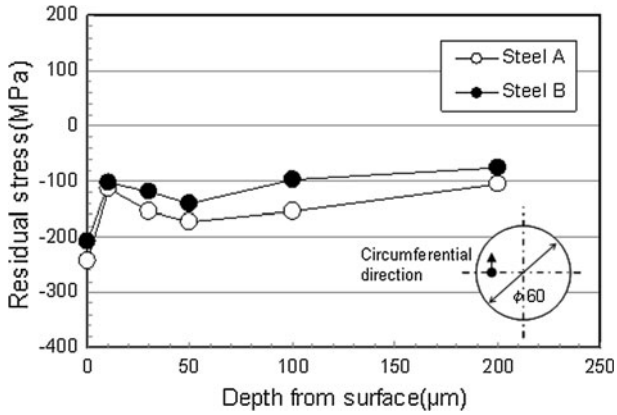

Fig. 5—Residual stress distribution of RCF test specimen.

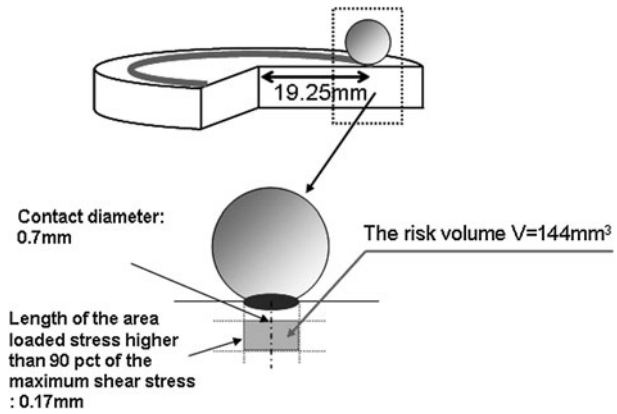

Fig. 6—Risk volume of RCF test specimen.

the shape of inclusion was different between steel A and steel B, the effect of residual compressive stress on the initiation and the propagation of rolling contact fatigue crack was almost the same.

B. *Inclusion Evaluation Methods*

Furuya *et al.*[30] proposed that the inclusion inspection method using ultrasonic fatigue testing can automatically and precisely detect most harmful inclusions in the inspection volume V_0 since the most harmful inclusions appear at the origin of fish-eye type fatigue fractures. According to this proposal method, the square root area, length, and width of inclusions that were observed at the origin on the fracture surface were measured. The maximum square root area, length, and width of inclusions in the target volume V of steels were estimated on the basis of statistics of extremes.[31]

The inspection volume V_0 is defined as the part of the ultrasonic fatigue test specimen suffering from stress higher than 90 pct of the maximum stress. The target volume V corresponds to the risk volume for 10 pieces of RCF test specimens. The risk volume of the RCF test specimen is determined by using the width of the rolling track and the depth of maximum shear stress as shown in Figure 6.

Ultrasonic fatigue tests for inclusion inspection were carried out using Shimadzu USF-2000 (Shimadzu Corporation, Kyoto, Japan). Fatigue test conditions were determined as follows.

Test frequency was 20 kHz, the stress ratio (R) was –1, and the number of cycles regarded as runout was over 1×10^8. If a specimen was regarded as runout, then the specimen was tested again under the stress level added over 10 pct. The stress level of the fatigue test was controlled with displacement measured at the open end of the specimen. Furthermore, an on–off test and cold air cooling were sometimes conducted in order to prevent the specimen from heatup.

Observation and analysis of inclusions on the fracture surfaces were carried out using a scanning electron microscope (SEM) and energy-dispersive atomic X-ray (EDAX). For the determination of the morphology of inclusions, the maximum length and maximum width were measured as shown in Figure 7. The maximum length of inclusions is parallel to the elongated direction of the forged bar and the maximum width of inclusions is along a perpendicular direction to the elongation.

C. *RCF Test Methods*

RCF tests were carried out using a thrust-type machine, as shown in Figure 8. Three balls moved on the specimen along the load axis. The ball diameter was 9.525 mm (3/8 in) and the material of the balls was JIS-SUJ2 (SAE52100 equivalent). RCF tests were conducted under the constant load (maximum value of Hertzian stress was 5.3 GPa) and rotating speed of 1000 rpm under well-controlled lubricant conditions. The surface roughness of the specimens, Ra, was about 0.02 μm. Nine specimens of each steel that contained two different shapes of MnS were tested. The RCF life was defined as the number of cycles to failure.

In order to identify the occurrence of RCF crack initiated from inclusions, SEM observation on the surface of the specimens was carried out after RCF tests.

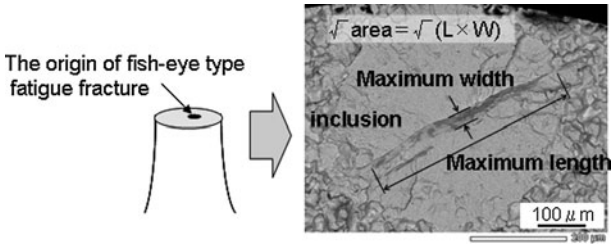

Fig. 7—Determination of the morphology of the origin of fish-eye type fatigue fracture.

III. RESULTS

A. *Shape of Inclusion*

The square root area, length, and width of inclusions that were observed at the origin of fish-eye type fatigue fractures were measured and have been plotted on Gumbel paper as shown in Figure 9. It was found that all inclusions observed at the origin of fish-eye type fatigue fractures in this ultrasonic fatigue test were MnS. According to these results, on the assumption that the most harmful inclusion to the RCF in both steels is MnS, the maximum MnS size for a target volume V (= 144 mm^3) of steel was estimated on the basis of statistics of extremes[31] using the fitted lines in Figure 9. The procedure is as follows:

$$\text{The maximum MnS size (the square root area, length and width)} = a \cdot y + b \cdots \quad (1)$$

$$y = -\ln(-\ln((T-1)/T)) \cdots \quad [2]$$

$$T = (V + V_0)/V_0 \cdots \quad [3]$$

where a and b are the fitted values on the Gumbel paper, shown in Figure 9, T is the return period, V_0 is the inspection volume, and V is a target volume of steel to estimate a maximum inclusion shape.

The maximum MnS square root area, length, and width estimated in a target volume V (= 144 mm^3) for each steel are shown in Table II. The maximum square root area and width for each steel were almost the same values. The maximum length in steel A was 1.4 times longer than that in steel B.

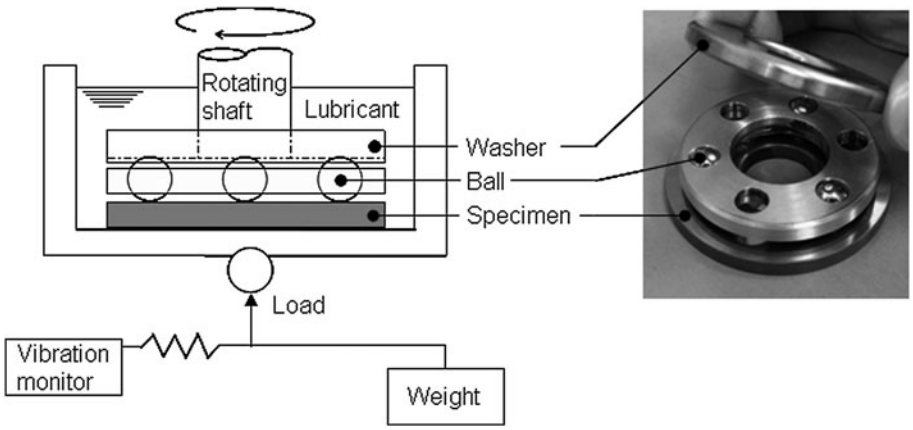

Fig. 8—Schematic illustration of thrust type RCF tester.

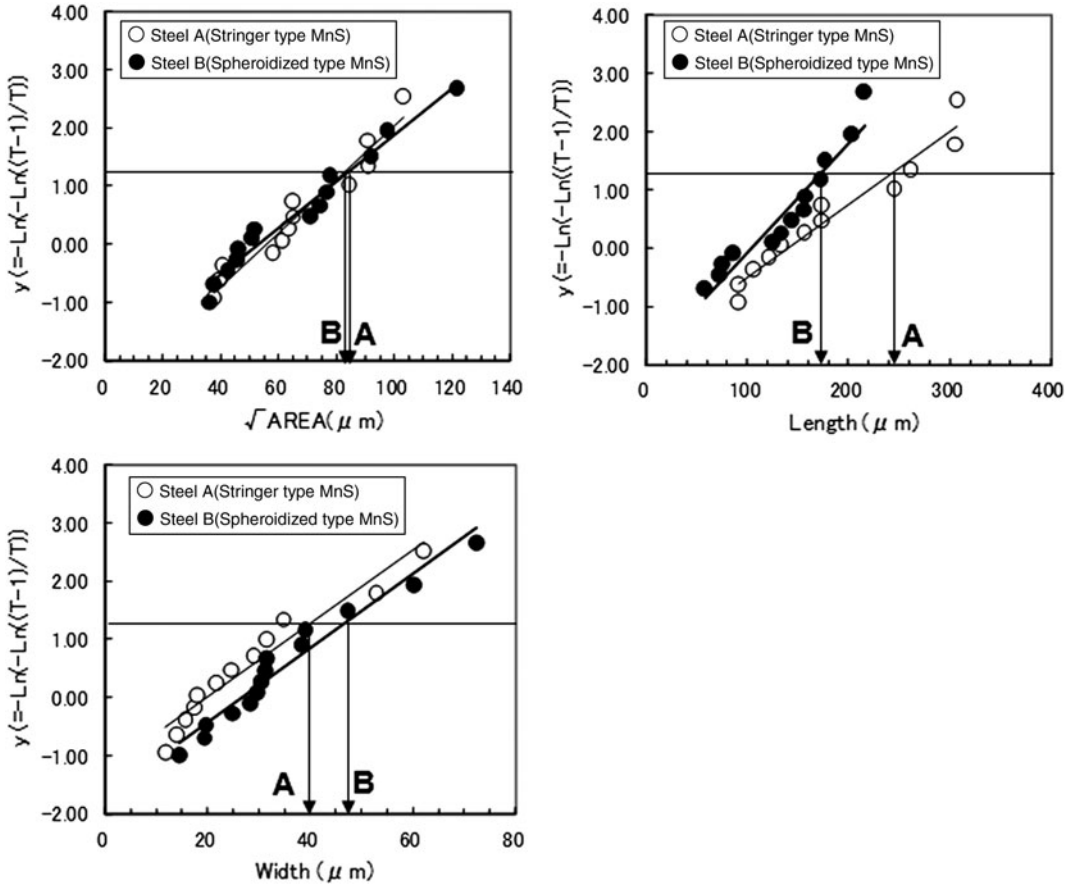

Fig. 9—Extreme distributions of inclusions at fracture origin.

Table II. Comparison of Maximum Size of Inclusions with RCF Lives

		Steel A	Steel B
Maximum size of inclusion estimated by statistics of extremes	$\sqrt{\text{area}}$*	84 μm	85 μm
	length	243 μm	171 μm
	width	40 μm	47 μm
RCF life	L10	3.29×10^6	4.67×10^6
	L50	4.07×10^6	1.14×10^7

B. *RCF Life*

Figure 10 shows the Weibull distribution of the RCF lives. To compare the RCF life with the maximum MnS size, L10 and L50 lives of each steel are shown in Table II, where L10 and L50 symbolize the lives that correspond to 10 pct and 50 pct of flaking failure, respectively. The Weibull distribution shows clearly that the RCF life of steel B containing spheroidized-type MnS was longer compared to that of steel A containing stringer-type MnS. The L50 life of steel B was about three times longer than that of steel A.

Nagao *et al.*[17] reported that maximum square root area of inclusions is one of the dominant factors affecting RCF life. Kizawa and Gotoh[27] and Hashimoto *et al.*[25] suggested that the maximum width of MnS, which represented the inclusion area projected to the plane parallel to the rolling contact plane, at the depth of maximum shear stress in RCF, was the dominant factor in RCF life when the oxides affect is eliminated.

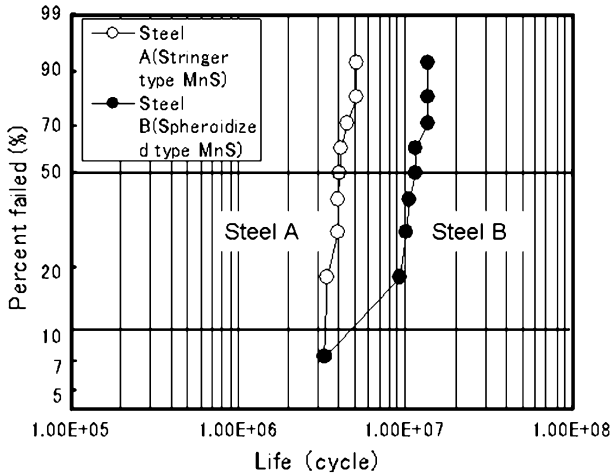

Fig. 10—Weibull distribution of RCF lives.

As shown in Table II, however, the remarkable difference of the maximum square root area and maximum width of MnS comparing steel A and steel B was not to be found. These results may indicate that the RCF life was well correlated with the maximum

length rather than the maximum square root area and maximum width of MnS, and the RCF life could be shortened as the inclusion length increased.

C. *Observation of RCF Crack Initiated from Inclusion*

To investigate the occurrence of RCF crack initiated from inclusions, SEM observation on the surface of the specimens was carried out after RCF tests. SEM images of cracks observed on the surface of specimens are shown in Figure 11. As shown in Figures 11(a) and (b), RCF cracks originating from MnS were observed on the surface in both steels. It should be noted that all these cracks observed in both steels were propagated to a direction perpendicular to the ball rolling direction. The width of the originated MnS was 30 μm for each steel. The wide length of the "perpendicular crack" of steel A was longer than that of steel B, although the number of cycles of steel A ($=3.4 \times 10^6$) was smaller than that of steel B ($=9.2 \times 10^6$).

It was well known that the local stress field was developed at the inclusion during the RCF test. Tensile stress in rolling direction was occurred near the surface of specimen, and shear stress in rolling and depth direction also occurred in subsurface of specimen. It seems that this perpendicular crack was initiated due to the tensile stress in rolling direction or shear stress in depth direction.

The shape of the originated MnS must affect the initiation and propagation behavior of these "perpendicular cracks" since the value of local stress would be changed due to the shape of inclusion.

To investigate the initiation and propagation behavior of these perpendicular cracks, the sectional observation was conducted. The results are shown in Figures 11(c) and (d). The features of the perpendicular cracks observed in the section were as follows.

In the section of steel A as shown in Figure 11(c), it was found that the perpendicular crack was propagated along the sidewall of the stringer-shaped MnS 150 μm in length and reached to the end of the stringer-shaped MnS.

While in the section of steel B as shown in Figure 11(d), the propagation behavior of the perpendicular crack was different from that of steel A. It was found that the perpendicular crack was initiated from spheroidized MnS and propagated to the depth direction. The length of the perpendicular crack initiated from spheroidized MnS reached 40 μm in depth, but its depth was shorter than that of the perpendicular crack initiated from stringer-shaped MnS.

Present results provided evidence suggesting a strong possibility that the propagation behavior of the perpendicular crack is well correlated with the length of the originated MnS because the value of tensile stress in rolling direction and shear stress in depth direction depends on the length of MnS. In other words, this result may support that the perpendicular crack grew acceleratory in mode I and mode III as the MnS length increased.

Next, attention was focused on the shear crack in the subsurface. The features of the shear crack in the subsurface observed in the section were as follows.

It was found that several shear cracks appeared parallel to the shear stress in rolling direction and were located at equal spacing in the section of steel A, as shown in Figure 11(c). The shear crack located at the depth of the maximum shear stress ($=100$ μm) was the longest.

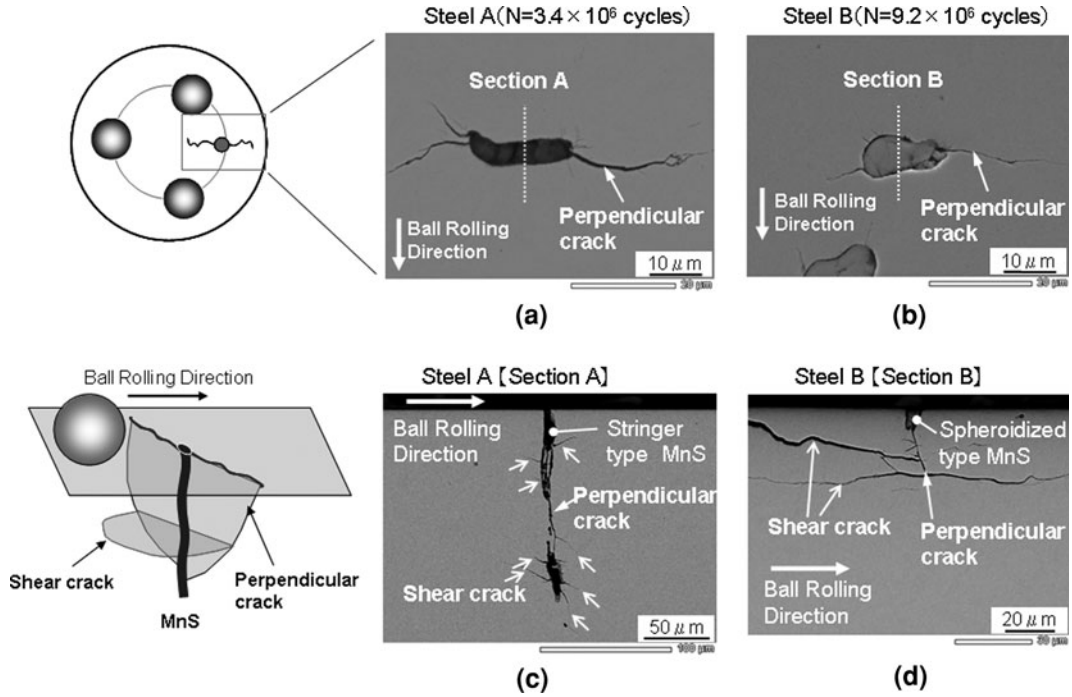

Fig. 11—SEM images of occurrences of RCF cracks.

However, in the section of steel B, it should be noted that shear cracks in the subsurface were initiated from the tip of the perpendicular crack, not from spheroidized MnS, and the depth of the occurrence of the subsurface crack was 40 μm from the surface, which was not reached at the maximum shear stress, as shown in Figure 11(d).

These results may suggest that the shear crack in the subsurface was initiated from the perpendicular crack and the wide-length of the perpendicular crack must dominate the initiation behavior of the shear crack in the subsurface.

Schematic illustrations of the formation of perpendicular and subsurface cracks are shown in Figure 12. The following assumption regarding the mechanism of the formation of RCF crack can be possible.

At the first stage of RCF (Figure 12(i)), the perpendicular crack was initiated at the region close to surface along inclusion due to tension in rolling direction and shear stresses in depth direction.

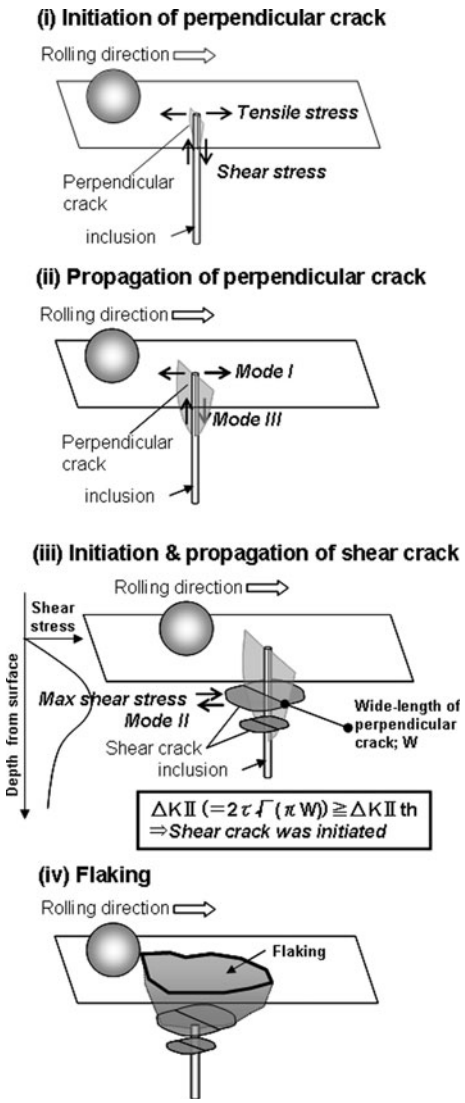

Fig. 12—Schematic illustration of RCF crack formation model.

And then, at the second stage of RCF (Figure 12(ii)), when the value of the stress intensity factor range in mode I (ΔKI) and mode III (ΔKIII) were more than the threshold value of the stress intensity factor range ($\Delta K\text{I}_{th}$, $\Delta K\text{III}_{th}$) respectively, the perpendicular crack was propagated in mode I and mode III to the depth direction.

The value of the stress intensity factor range in mode I (ΔKI) and mode III (ΔKIII), which calculated by using the tensile stress in rolling direction and shear stress in depth, respectively, would be increased depending on the length of inclusion. That means the perpendicular crack grew acceleratory as the MnS length increased.

Next, at the third stage of RCF (Figure 12(iii)), when the value of the stress intensity factor range in mode II ($\Delta\text{KII} = \Delta\tau \times (\pi W)^{0.5}$) calculated by using both the shear stress τ and the wide-length of the perpendicular crack W at a certain depth was more than the threshold value of the stress-intensity factor range in mode II($\Delta K\text{II}_{th}$), the shear crack in the subsurface was initiated from the position of $\Delta K\text{II} > \Delta K\text{II}_{th}$. Of course, the propagation of the perpendicular crack to the depth direction continued, therefore several shear cracks appeared and were located at equal spacing in the section.

Finally, the main shear crack locating the direction of maximum shear stress was propagated and caused the flaking failure (Figure 12(iv)). The validity of this hypothesis will be verified in the next section.

IV. DISCUSSION

To verify the assumption regarding the mechanism of the formation of RCF crack experimentally, the RCF tests of steel A were interrupted at $N = 1 \times 10^4$, 1×10^5, and 1×10^6 cycles before flaking failure. Sectional observation procedure was the same manner as mentioned in the previous section.

In addition, to confirm the origin of RCF, the fractographic study of the specimen occurring the

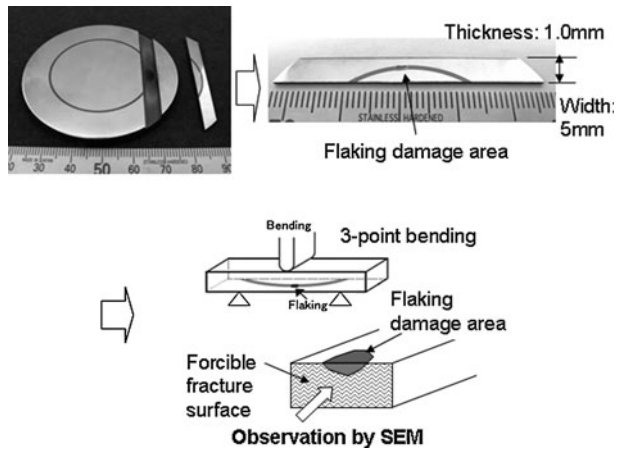

Fig. 13—Experimental procedure of fractographic study of flaking failure.

flaking failure was also carried out according to the evaluation method that Nagao *et al.* suggested.[17] The experimental procedure for the fractographic study of flaking failure is shown schematically in Figure 13. As shown in Figure 13, the three-point bending test specimen, in which the flaking damage area was located in the center of the specimen surface, was cut off from the RCF specimen. The flaking damage area was forcibly divided by pulling force of three-point bending, and fracture surface observation was carried out using SEM.

The sectional observation results of interrupted specimens are shown in Figure 14. It was confirmed that no shear crack in the subsurface could be observed in the section of both specimens interrupted at 1×10^4 cycles and 1×10^5 cycles, although the perpendicular crack initiated from MnS appeared in both specimens, as shown in Figure 14.

Courbon *et al.*,[32] Kabo,[24] and Alley and Neu[19] tried to determine the local stress concentration caused around inclusion by using numerical simulation. For example, Courbon et al.,[32] suggested that the stress concentration dramatically change as the inclusion orientation and shape in rolling contact, and the endurance limit of bearing steel was decreased when the axis of stringer type of inclusion was close to the normal to the contact surface.

As shown in Figure 14, the perpendicular crack was initiated at the region close to a surface along the stringer-shaped MnS axed perpendicular to the contact surface. It means the perpendicular crack nucleation was appeared with increasing local tensile and/or shear stress concentration depending on the shape of MnS.

On the other hand, in the section of the specimen interrupted at 1×10^6 cycles, several shear cracks in the subsurface were observed.

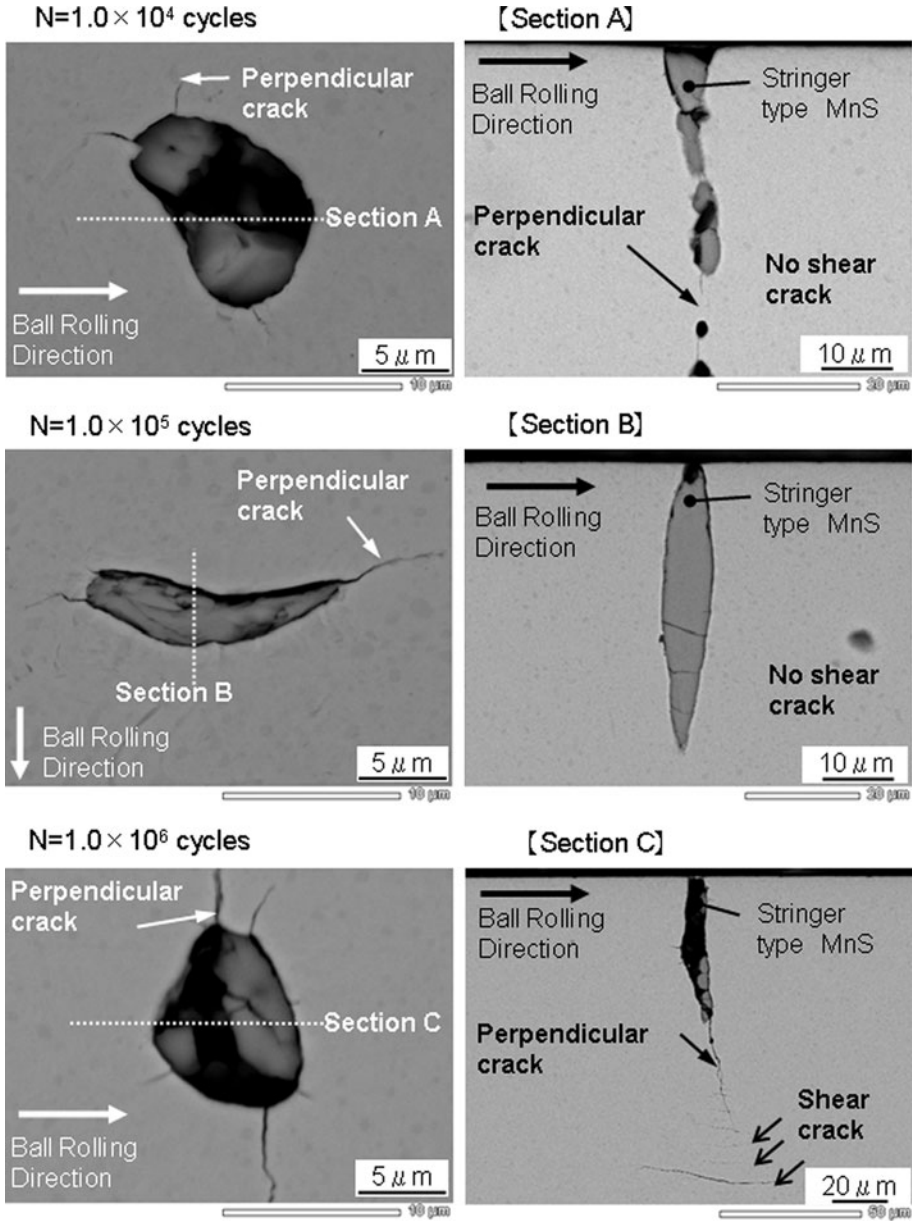

Fig. 14—SEM images of occurrences of RCF cracks of interrupted specimens.

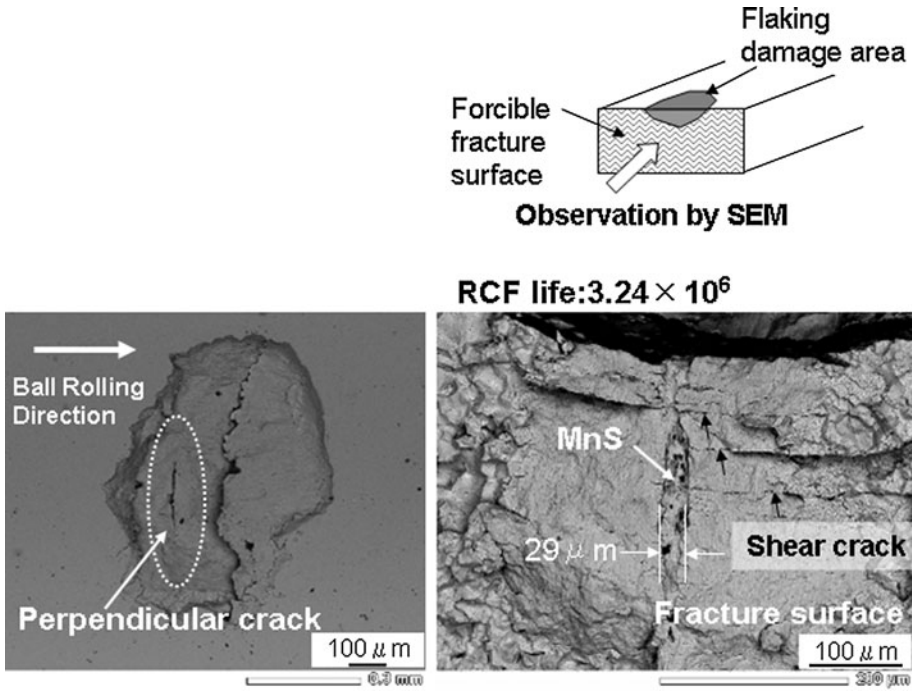

Fig. 15—SEM images of flaking damage area and forcible fracture surface.

Furthermore, SEM images of the flaking damage area and the fracture surface of the flaking area divided forcibly by three-point bending are shown in Figure 15. The perpendicular crack existed at the bottom of the flaking, and the flaking damage area was divided from this perpendicular crack by three-point bending.

It was found that the elongated MnS with a maximum width of 10 μm, assumed as the origin of RCF, existed at the center of the fracture surface related with the perpendicular crack, and several shear cracks located at equal spacing were observed in the fracture surface. These results were in good agreement with the hypothesis. Therefore, it was concluded that the initiation behavior of shear crack in the subsurface was well correlated with the propagation behavior of the perpendicular crack. The results of this study indicated that reduction of inclusion length is one of the most important factors to improve the RCF life.

Further and more precise analysis of local stress field in RCF due to the shape of inclusion, especially the length of inclusion, by using FEM is necessary to reach a conclusion, but this experimental result may indicate the direction of further research work to clarify the mechanism of the initiation and propagation of RCF crack.

V. CONCLUSIONS

This study evaluated the influence of the inclusion shape on the RCF life by using carburized JIS-SCM420 (SAE4320) steels that contained two different shapes of MnS as inclusions.

The results are summarized as follows:

1. Two different types of fatigue cracks—perpendicular crack and shear crack—were induced in RCF.
2. The perpendicular crack was initiated from MnS and the propagation of the perpendicular crack was well correlated with the length of MnS.
3. This reason was assumed that the value of the stress intensity factor range in mode I (ΔKI) and mode III (ΔKIII), which calculated by using the tensile stress in rolling direction and shear stress in depth, respectively, would be increased with the length of inclusion, and as a result, the perpendicular crack grew acceleratory in mode I and mode III as the MnS length increased.
4. The shear crack was initiated from the perpendicular crack, and the initiation of shear crack governing the RCF life varied depending on the propagation of the perpendicular crack.
5. RCF life was well correlated with the length of MnS since the initiation of shear crack in the subsurface was accelerated as the length of MnS increased. The results of this study indicated that reduction of inclusion length is one of the most important factors to improve the RCF life.

REFERENCES

1. G. Lundberg and A. Palmgren: *Acta Polytech. Mech. Eng.*, 1947, vol. 1, p. 3.
2. T. Uesugi: *Trans. Iron Steel Inst. Jpn.*, 1988, vol. 28 (11), pp. 893–99.
3. G. Akashi, K. Doi, Y. Matsushima, I. Takagi, and Y. Fukuzaki: *Wire J. Int.*, 1999, vol. 32 (8), pp. 92–97.
4. D. Nelias, M.L. Dumont, F. Champiot, A. Vincent, D. Girodin, R. Fougeres, and L. Flamand: *Trans. ASME J. Tribol.*, 1999, vol. 121 (240), pp. 240–51.
5. P.C. Becker: *Met. Technol.*, 1981, vol. 8 (6), pp. 234–43.

6. A. Kerrigan, J.C. Kuijpers, A. Gabelli, and E. Ioannides: *J. ASTM Int*., 2006, vol. 3 (6), pp. 101–06.
7. W.E. Littman and R.L. Widner: *Trans. ASME J. Basic Eng*., 1996, vol. 88 (3), pp. 624–36.
8. A. Vincent, G. Lormand, P. Lamagnere, L. Gosset, D. Griodin, G. Dudragne, and R. Fougeres: *Bearing Steel into the 21st Century*, J.J.C. Hoo, ed., ASTM International, West Conshohocken, PA, 1988, pp. 109–23.
9. I.J. Davies, M.A. Clarke, and D. Dulieu: *Bearing Steel into the 21st Century*, J.J.C. Hoo, ed., ASTM International, West Conshohocken, PA, 1988, pp. 375–89.
10. D. Girodin, G. Dudragne, J. Courbon, and A. Vincent: *J. ASTM Int*., 2006, vol. 3 (6), pp. 85–100.
11. P. Trady, L. Tolnay, Gy. Károly, and J. Mezei: *Proc. 6th Int. Iron and Steel Cong*, ISIJ, Nagoya, Japan, 1990, p. 629.
12. T. Lund and J. Akesson: *ASTM Spec. Tech. Publ., No. 987*, J.J.C. Hoo, ed., American Society for Testing and Materials, West Conshohocken, PA, 1988, p. 308.
13. Y. Kurebayashi, K. Namiki, T. Shibata, and M. Takagi: *CAMP ISIJ*, 1989, vol. 2, p. 1976.
14. A. Melander: *Int. J Fatigue*, 1997, vol. 19, pp. 13–24.
15. K. Hashimoto, T. Fujimatsu, N. Tsunekage, K. Hiraoka, K. Kida, and E.C. Santos: *Mater. Des*., 2011, vol. 32, pp. 4980–85.
16. T. Fujimatsu, M. Nagao, M. Nakasaki, and K. Hiraoka: *Sanyo Tech. Rep*., 2006, vol. 13 (1), pp. 62–66.
17. M. Nagao, K. Hiraoka, and Y. Unigame: *Sanyo Tech. Rep*., 2005, vol. 12 (1), pp. 38–45.
18. D.L. McDowell: *Mater. Sci. Eng. A*, 2007, vol. 468-70, pp. 4–14.
19. E.S. Alley and R.W. Neu: *Int. J. Fatigue*, 2010, vol. 32, pp. 841–50.
20. E.S. Alley, K. Sawamiphakdi, P.I. Anderson, and R.W. Neu: *J. ASTM Int*., 2010, vol. 7 (2), pp. 1–20.
21. R. Prasannavenkatesan, J. Zhang, D.L. McDowell, G.B. Olson, and H. Jou: *Int. J. Fatigue*, 2009, vol. 31, pp. 1176–89.
22. J. Zhang, R. Prasannavenkatesan, M.M. Shenoy, and D.L. McDowell: *Eng. Fract. Mech*., 2009, vol. 76, pp. 315–34.
23. A. Stienon, A. Fazekas, J.Y. Buffiere, A. Vincent, P. Daguier, and F. Merchi: *Mater. Sci. Eng. A*, 2009, vols. 513–514, pp. 376–83.
24. E. Kabo: *Int. J. Fatigue*, 2002, vol. 24, pp. 887–94.
25. K. Hashimoto, K. Hiraoka, and K. Kida: *CAMP ISIJ*, 2010, vol. 23, p. 430.
26. K. Hashimoto, K. Hiraoka, and K. Kida: *TMS2011 140th Annual Meeting & Exhibition*, San Diego Convention Center, San Diego, CA, 2011.
27. K. Kizawa and M. Gotoh: *Koyo Eng. J*., English Edition, 2003, no. 163E, p. 37.
28. K. Furumura and K. Hirakawa: *NSK Tech. J*., 1979, vol. 638, pp. 1–13.
29. K. Hashimoto, K. Hiraoka, K. Kida, and E.C. Santos: *Mater. Sci. Technol*., 2012, vol. 28 (1), pp. 39–43.
30. Y. Furuya, S. Matsuoka, and T. Abe: *Metall. Mater. Trans. A*, 2003, vol. 34A, pp. 2517–26.
31. Y. Murakami: *Metal Fatigue: Effects of Small Defects and Nonmetallic Inclusions*, Elsevier, London, U.K., 2002.
32. J. Courbon, G. Lormand, G. Dudragne, P. Daguier, and A. Vincent: *Tribol. Int*., 2003, vol. 36, pp. 921–28.